Electrically injected metamaterial grating DFB laser exploiting an ultra-high Q electromagnetic Induced Transparency resonance for spectral selection

Natalia Dubrovina, Yaoyao Liang, Quentin Gaimard, Vincent Brac de la Perrière, Kamel Merghem, Henri Benisty, André de Lustrac, Abderrahim Ramdane, Anatole Lupu

Electrically injected metamaterial grating DFB laser exploiting an ultra-high Q Electromagnetic Induced Transparency resonance for spectral selection

Natalia Dubrovina, Yaoyao Liang, Quentin Gaimard, Vincent Brac de la Perrière, Kamel Merghem, Henri Benisty, André de Lustrac, Abderrahim Ramdane, and Anatole Lupu

N. Dubrovina, Y. Liang, Q. Gaimard, V. Brac de la Perrière, K. Merghem, A. De Lustrac, A. Ramdane, A. Lupu
Centre de Nanosciences et de Nanotechnologies, CNRS, Université Paris-Saclay, C2N – 10 Boulevard Thomas Gobert – 91120 Palaiseau cedex, France
E-mail: anatole.lupu@c2n.upsaclay.fr

N. Dubrovina
now with Almae Technologies, Site Data 4, Route de Nozay, 91460 Marcoussis, France

Q. Gaimard
now with Laboratoire de physique des lasers, Université Sorbonne Paris Nord (USPN) - Institut Galilée - CNRS LPL UMR7538 99, av. J.B. Clément - 93430 Villetaneuse – France

K. Merghem
Telecom SudParis, Institut Polytechnique de Paris, 91120 Palaiseau, France

A. de Lustrac,
LEME, UPL, Univ Paris Nanterre, F92410 Ville d'Avray, France

H. Benisty
Laboratoire Charles Fabry, Université Paris-Saclay, Institut d'Optique IOGS, 2 Avenue A Fresnel, 91120 Palaiseau, France

Keywords: Electromagnetically Induced Transparency, Fano resonances, metamaterials, DFB lasers

We show that, in waveguide (WG) configuration, the coupling of a 2D plasmonic metamaterial grating (MMG) having conventional Bragg period along the guide but a distinct period along the transverse axis can lead to Electromagnetically-Induced-Transparency (EIT) behavior. This supports the idea that metamaterials, as functional photonic building blocks, can lead to low losses in many standard devices if properly designed. We report the observation in passive WGs of a marked Fano type EIT effect with record high quality factor of resonance: Q~5000 and contrast >20dB. Unlike any standard metal grating, MMG assisted waveguides exhibit both strong grating coupling strength and low-loss properties simultaneously. This concept is further applied to the demonstration of single frequency emission electrically injected DFB lasers in the NIR telecom domain. The key point is that laser emission occurs at the peak of EIT, i.e. the maximum in transmission. It addresses in this way one of the main critical issues of DFB lasers related the single frequency yield. The laser performances are at the state-of-the art (I_{th}<20mA, P_{max}>20mW at I=200mA, SMSR>50dB, tolerance to optical feedback > -21dB compliant with IEEE 802.3 standard). The presented approach is compatible with existing industrial technologies and promising for real-life telecom applications.

1. Introduction

Metamaterials (MMs) exploit the emerging properties of an array of individual elements displaying some kind of resonance, with the scope of producing artificial photonic responses absent from normal materials.[1-12] The form of a 2D array has often been considered for obvious feasibility reasons, with basic features such as near-normal incidence transmission/reflection exhibiting a host of new effects. The popular word of "metasurfaces" commonly refers to the most of such 2D arrays. Waveguides (WG), which are a privileged vehicle of functional photonics, have also been considered with MMs.[13-21] However, since metallic/plasmonic structures often constitute the elementary MM resonators, the incurred losses, to which guided modes are quite sensitive, have been a substantial hurdle to the achievement of convincing and broad-reaching demonstrations.

The strategy to exploit a MM response while minimizing losses is to strongly abate the relevant modal field precisely when the desired metamaterial working point is reached, at some specific point of its collective resonance. Electromagnetically induced transparency (EIT) and a variety of related Fano resonances articulate this strategy.[22-34] They have undoubtedly paved the way toward the present demonstration. EIT is a universal effect,[22-23] arising with three oscillators (atoms, cavity modes, guided modes …) when amplitudes and coupling of two of them cause a zero amplitude of the third one, whose only apparent role at such condition is to transfer amplitude. For this simple reason, any loss mechanism affecting the third oscillator in isolation nearly vanishes in the EIT regime: in a nutshell, no field build-up, no losses, but nevertheless a large amplitude transfer. The origin of this EIT can alternatively be related to destructive/constructive Fano interference effects due to the presence of two possible pathways for the scattered wave, hence a negligible dissipation, causing a sharp spectral peak to appear in the middle of a broad transmission dip.

In this paper, we show that the classical counter-directional Bragg coupling in a WG, which usually results in a single narrow-band transmission dip for small periodic modulations of the WG's refractive index profile (the "distributed" grating of DFB [Distributed FeedBack] lasers and DBR [Distributed Bragg Reflectors] devices with dielectric or metallic type gratings, is amenable to the EIT strategy through a MM array of the cut-wire type. We demonstrate that when varying the cut-wires length l and thus the MM-mediated resonance of the third mode, the EIT feature is strongly modulated. Specifically, the MM itself is a duplicate array of cut-wire with a longitudinal period apt for conventional feedback (here at frequency $\nu \sim 200$T Hz, or $\lambda \sim 1.5\,\mu$m), sitting on either side of a ridge waveguide whose vertical guidance is classically ensured by a high-index layer embedded beneath the device surface. It shall be argued that this structure supports two kinds of modes that are coupled. Firstly, it supports channel-guided forward and backward modes, that undergo traditional coupling and feedback due to the fact that their lateral tail overlaps the MM periodicity, without any specific role of its plasmons. Secondly, it supports modes that also propagate forward and backward along the device longitudinal axis, but mostly in the MM areas. They are built from the localized resonances of the MM wires, but already hybridized with the near-planar guided mode below. Their coupling with the channel-guided modes is responsible of the appearance of the EIT in the channel-guided modes. The novel EIT-type feedback thus realized is supported by a simplified coupled-mode model.

This concept is further applied to the demonstration of single frequency emission electrically injected DFB lasers exploiting a resonant enhanced transmission due to the EIT first at $\lambda \sim 1.24\mu$m, then at $\lambda \sim 1.55\mu$m. It addresses in this way one of the main critical issues of DFB lasers, specifically the single frequency yield. Thus for index coupled DFB lasers a significant part of fabricated laser diodes show a dual frequency behavior with laser emission occurring either at the lower or higher frequency edge of the Bragg grating stop-band. The conventional approach for index coupled DFB lasers to get their lasing wavelength occuring at exact Bragg wavelength λ_{Br} is to use a quarter-wavelength phase shifter section of length

Λ/2 inserted in the middle of the laser cavity and also small facets reflectivities (R<1%).[35-37] However, the accompanying increase of the cavity mirror related losses results in a higher threshold gain, which is extremely undesirable. Besides, this solution entails the advent of spatial hole burning at the laser center, which impacts several laser specifications.

Greatly enhanced single-mode yield when introducing imaginary-coupling (gain or loss) was demonstrated throughout the 90s. Owing to their proven higher immunity to facets reflection, gain-coupled DFB lasers further attracted a lot of interest with the hope of a lower sensitivity to any optical feedback.[38,39] This sensitivity was indeed found to decrease with increasing coupling strength and the facets reflectivity. But this implied that a highly absorptive grating should be used. For instance, coupling coefficients around 5-20 cm^{-1} could be attained using chromium grating ($\kappa L \sim 0.25–1$ for 500-μm-long DFB lasers).[40] However, there are several factors limiting the coupling strength of such metallic Bragg gratings. The more serious one is that introducing higher loss modulation in the system also means an increased average loss, which augments noise and unavoidably requires a higher gain level, thus resulting in increased threshold current density.[41,42] Another drawback is the negligible polarization selectivity of such Bragg gratings. Polarization selection then requires specific strain engineering of gain media that introduces additional complexities.

For the DFB lasers considered in this work, the MMG plays the role of the third wave coupling the two others, but without field build-up at the favorable condition. This remarkable feature means in other words that the standing wave interference between the two counter-propagating modes manages to cancel out the electric field at the plasmonic nanoresonator, reminiscent of the bound states in the continuum (BIC) mechanism.[43] In agreement with recent theoretical predictions,[44] MMG assisted waveguides exhibit both slow-light (amplitude is exchanged with the counter-propagating modes) and low-loss properties simultaneously, largely at variance with any standard metal grating.

The occurrence of EIT in a MMG assisted waveguide brings a lot of advantages that may trigger a new paradigm for DFB lasers. The most important advantage is that the high density of photonic states favoring laser action is also accompanied by a maximum in transmission which is distinctly higher as compared to the rest of the spectral response. Other important advantages brought by the MMG DFB laser concept are:

- Large single-mode yield: The expected single mode laser operation is a direct consequence of the high density of states and low loss EIT combination, easing immunity to facets reflectivity and package feedback.
- Low threshold current: The operation at the EIT point strongly reduces the losses associated with the presence of metallic nanoparticles and requires less threshold gain to start laser emission.
- Increased grating strength: There are two factors allowing the desirable increase of the grating strength: i) Reduced Joule losses associated with EIT makes possible to increase by an order of magnitude the effective (longitudinally averaged) overlap of the guided wave with the MMG; ii) For a given overlap the grating strength can be approximately increased by one order of magnitude due to the resonant properties of metamaterial nanowires (~quality factor Q). Our results obtained on passive type structures (see next section) show an order of magnitude increase of MMG strength as compared to a conventional metallic Bragg grating like. This extra strength brings a more sturdy device coherence.
- Miniaturization and compactness: As follows directly from the point above the size of the laser cavity can be reduced proportionally to the grating strength. This opens promising prospects for highly miniaturized laser sources that are in high demand for III-V/SOI hybrid integration applications, either for distribution networks or inside connection-hungry data centers.

- Polarization selectivity: The resonant properties of metamaterial nanowires are strongly dependent on the polarization of the propagating wave. Our experimental results obtained on passive type structures show 15 dB of optical feedback selectivity between TE and TM polarizations.

The article is organized as follows. In Section 2 we describe the passive MMG waveguide structures operating at wavelength $\lambda > 1.45\ \mu m$ and show the main spectral properties observed, i.e. an ultra-high quality factor EIT resonance due to WG modes interacting with the MM resonant mode. Section 3 describes the coupled-mode model used to reproduce the typical EIT-type spectra. The Section 4 is dedicated to the description of electrically injected MMG FDB lasers whereby the same waveguide structure is used for the demonstration of laser emission associated with the EIT at $\lambda \approx 1.24\ \mu m$ wavelength. The adaptation of the waveguide and MMG design to a more conventional DFB laser for operation at 1.55 µm and an overview of the preliminary obtained performances are also presented. The final Section 5 summarizes the obtained results and draws future prospects.

2. Demonstration of EIT in passive MMG assisted guided wave structures

The WG and MMG investigated in this study are schematically depicted in **Figure 1**. The WG vertical basis consists of a core of 14 GaAs/$In_{0.15}Ga_{0.85}As$/InAs periods with the alloy growing into quantum dots and total thickness of 456 nm sandwiched between $Al_{0.35}Ga_{0.65}As$ layers. This choice was motivated by the possibility of using the same heterostructure for the fabrication of either passive or active devices. Indeed, since the emission of quantum dots is around $\lambda \approx 1.24\ \mu m$, above 1.3 µm wavelength, the core guiding active region is transparent and can be used for transmission measurements on passive waveguides. To define a channel waveguide, a 2-µm-wide deep-ridge with a rectangular profile is etched in the top cladding down to an etch-stop layer that leaves a flat surface. Its height is 1.5 µm. The channel WG mode pinned by the dip ridge is shown schematically in Figure 1. Its effective index is denoted $n_{eff}(\lambda)$. It protrudes in the ridge and gently overlaps the horizontal air-free surface at the sides of the ridge.

The symmetric duplicated MM arrays are elaborated on these flat outer surfaces. Each array consists of 6 to 8 cut-wires, periodically repeated along the WG propagation axis with a longitudinal period $\Lambda_z = \lambda / 2n_{eff}$ (targeting ν~200 THz, thus λ~1500 nm). The first effect of these wires is that the innermost one can naturally cause a conventional Bragg feedback between the two WG counter-propagating modes due to the periodic modulation of $\varepsilon(x, y, z)$ along z. In addition a generic cut-wires array displays a resonant behavior that strongly depends on the size of the wire (length l and cross-section $h \times w$ and of the size g of the gaps between the wires. However, the collective mode that would be solely derived from the plasmonic behavior of the wires (here gold wires) would still suffer large propagation losses along z, and would in general be difficult to phase-match to a WG mode. The presence of the core layer everywhere beneath the cut-wire arrays means that we must consider the hybridized mode of the array with the set of core-layer-supported modes propagating also along z. The fundamental lateral x mode profile of the MM system is the symmetric one that is pictured in Figure 1, which can be seen as the degenerate combination of two identical MM modes, one on each side, each with a lateral extent similar to the MM lateral extent of 1.5 to 2 µm as will be seen from the transverse MMG period $\Lambda_x = l + g \sim 225 - 300$ nm values and the amount of 6-8 wires used.

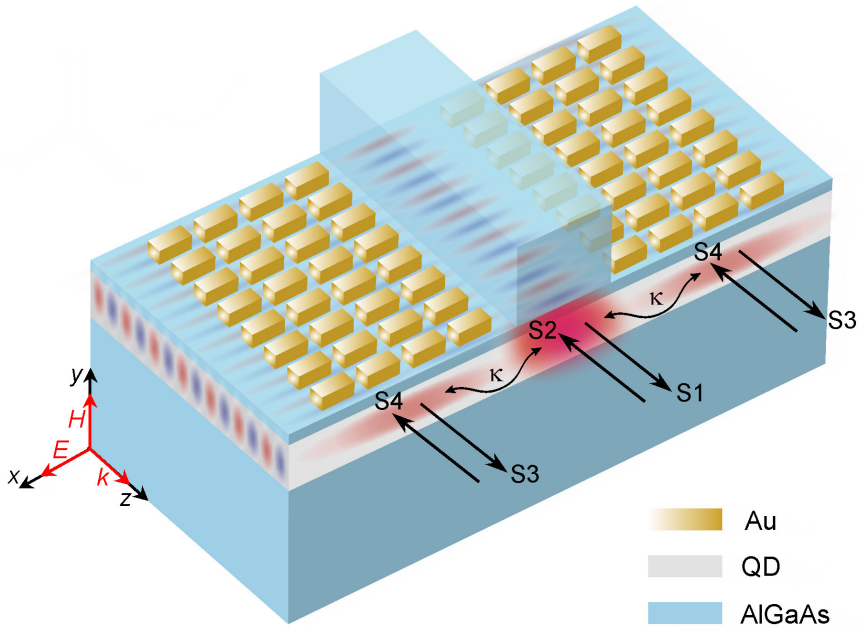

Figure. 1 Sketch of the dielectric ridge waveguide assisted by MM Bragg grating. The arrows S_1 and S_2 represent the two counter-propagating modes of the ridge waveguide. The arrows S_3 and S_4 represent the fundamental plasmonic supermode of the MM grating. Their profiles (blue/red/brown) are visible on the different cuts.

In this way the hybridized modes can have only a minority plasmonic character and a reasonable chance to be near-phase-matched to the WG modes, and thus to play the role of a third mode having overall a similar nature in terms of effective index and Bloch mode structure but nevertheless a substantial resonant contribution due to the cut-wire array. At the present stage, we will use "MM" to describe either the cut-wire array or the actual hybridized mode in the following. It entails no ambiguity as long as we do not attempt to break down the hybridized mode in its "constituents".

A SEM view of experimentally realized MMG waveguide is shown in **Figure 2a**. As for the rest of the experimental preparation, we used laser diode fabrication techniques to obtain bars of similar ridges with different $\Lambda_x = l + g$ values located aside each other. They are cleaved to a common sample (bar) length of ~3 mm with the mirror cleaved facets left uncoated. The size of the gap between metallic wires $g = \Lambda_x/3$ while their length $l = 2\Lambda_x/3$ spans from 150 to 200 nm by 10 nm steps. Two control samples, one with a conventional Bragg metallic grating and the other without any MMG (a simple Fabry-Perot (FP) cavity formed by WG with cleaved facets), were also included. Since these passive devices are dedicated to spectral transmission measurements, they were not protected or passivated.

The transmission measurements were made with a tunable laser sources Tunics+, with $\Delta\lambda$=2 pm wavelength spectral resolution. Details on the experimental characterization techniques used for this study are presented in Section S1 (Supporting Information). The experimental spectral response represented in Figure 2b for a 3.2 mm long MMG ridge waveguide shows the presence of a marked EIT at 1607 nm. As can be seen, the peak value of transmission is more than 2 dB higher with respect to the WG transmission level outside the EIT resonance. This behavior is distinctly different from that of conventional metallic Bragg grating WG shown in Figure 2c, whose spectral response is represented in Figure 2d. As can be seen, in this case only a transmission dip corresponding to the absorption+reflection at the Bragg wavelength is observed. Note also that this dip around 5 dB is much shallower

compared to that observed for the MMG WG, proving thus our assertion on the increase of the grating strength.

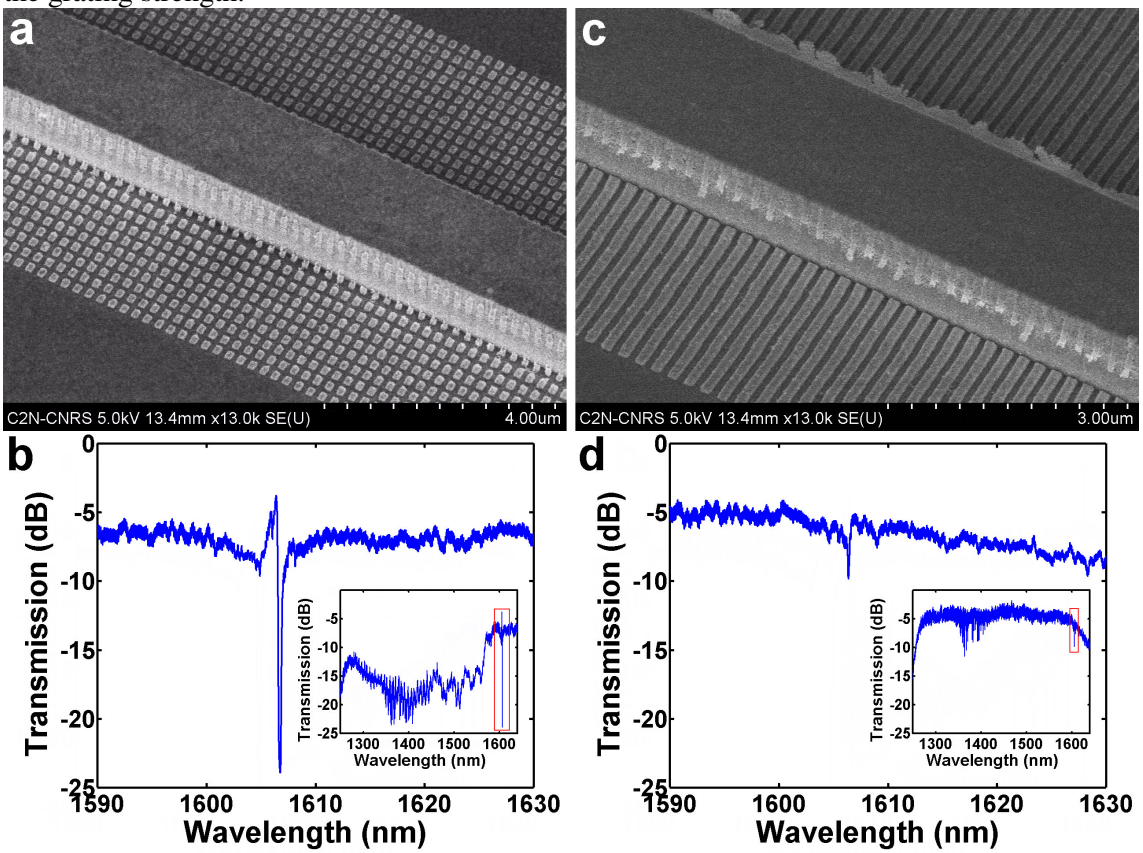

Figure 2. a) SEM view of gold cut-wires MMG and III-V passive semiconductor waveguide. b) Transmission spectrum of a 2 µm wide and 3.2 mm long MMG ridge waveguide in the EIT region. The inset shows the spectral response at extended wavelength range. The red box indicates the EIT region. MMG parameters used in considered design: Λ_z=250 nm, Λ_x=270 nm and gold cut-wires dimensions $l=180$ nm, $w=120$ nm, $h=50$ nm. c) SEM view of metallic (Au) Bragg grating assisted passive semiconductor waveguide with period Λ_z=245 nm. d) Transmission spectrum of 3.2 mm long metallic Bragg grating Λ_z=250 nm, ridge waveguide.

The increase of the MM grating strength can also be inferred by the observation of a 10 dB trough in a broad transmission range below 1570 nm in the enlarged spectrum shown as an inset in Figure 2b. It corresponds to the slowly variable coupling to radiation modes in the lateral continuum, remaining essentially smooth down to 1300 nm. The drop in transmission below this wavelength is due to the absorption of quantum dots which is maximum around 1.24 µm. This fact further supports the arguments according to which the coupling force of the conventional metallic Bragg grating with otherwise identical parameters is much weaker than that of its MMG counterpart, thus opening the way to further miniaturizations of this type of devices.

Next, for a shorter longitudinal period $\Lambda_z = 230\,\text{nm}$, we investigate the role of MMG cut wires length l as it is varied from 170 to 190 nm by steps of 10 nm. For ridge WG the effective index $n_{\text{eff}} = 3.226$ and the Bragg wavelength $\lambda_{Br} = 2n_{\text{eff}}\Lambda_z = 1484$ nm. The corresponding spectral responses in the EIT region are represented in **Figure 3a**. As can be seen, the EIT-related features are more marked as the cut-wires length is increased. This general trend can

be attributed to the shift of the localized surface plasmons resonance (LSP) toward higher wavelengths that enhances the magnitude of the EIT when it becomes closer to that of the Bragg wavelength. To verify this assumption we explore the spectra when tuning the frequency of cut-wires resonances by adding a water droplet on the surface of MMG WG. In this configuration, as can be seen in Figure 3b, the EIT-related features are more marked even for the shortest $l = 170$ nm. The $l = 190$ nm case is still the more marked in terms of EIT "shape", falling heuristically in the middle of an absorption trough, but the top transmission is affected. Note that the half-width of the EIT peak for $l = 190$ nm in Figure 3b is approximately 0.3 nm, which corresponds to a resonance quality factor Q ~ 5000. This is the highest value reported so far for NIR domain MM, especially when taking into account that the length of the MMG WG is very long around 3.2 mm. The interplay of guidance and MM resonance are key to the obtainment of such a high value, it is not a characteristic that the isolated array would display. This point will be supported by the modelling.

A similar situation holds when considering MMG WGs with longitudinal period $\Lambda_z = 250$ nm and $\lambda_{Br} = 1607$ µm. The corresponding spectral responses for an "air-clad" MMG WG and the water clad one are represented in Figure 3c and 3d, respectively. We observe that the onset of EIT takes place at the lower $l = 150$ nm value. We attribute this feature to the higher gold conductivity of the cut-wires at the longer wavelength and the smaller ratio of skin depth to feature size. Also note that the contrast of the EIT peak is very high. For instance for the data presented on Figure 3c when the MM cut-wires length $l = 180$ nm, it reaches up to 20 dB, and could still be limited by extrinsic experimental factors. Such narrow band and record high contrast features may be especially interesting for sensing applications. They could also address the spectral management of amplified spontaneous emission ASE in diode lasers.

This latter characteristic is due to the contrast in absorption around the immediate vicinity of the EIT peak. The impact of this loss modulation best appears for the length of the cut wires $l = 170$ nm in the transmission spectra displayed on Figure 3a and 3c. The amplitude of the FP oscillations decreases toward the peak of the EIT, damping in this way all cavity longitudinal modes in the EIT region except the one at the EIT peak.

Taking a global view, the common features of the set of results points toward the universal character of the observed EIT response, provided some tuning of the MMG is adequately performed. Note, finally, that this EIT effect is observed only for TE light polarization, i.e. when the electric field component is oriented along the x-axis. It is absent in the case of TM polarization, i.e. when electric field component is along y-axis. Additional discussion related to the polarization selectivity properties of MMG are provider in Section S1 (Supporting Information).

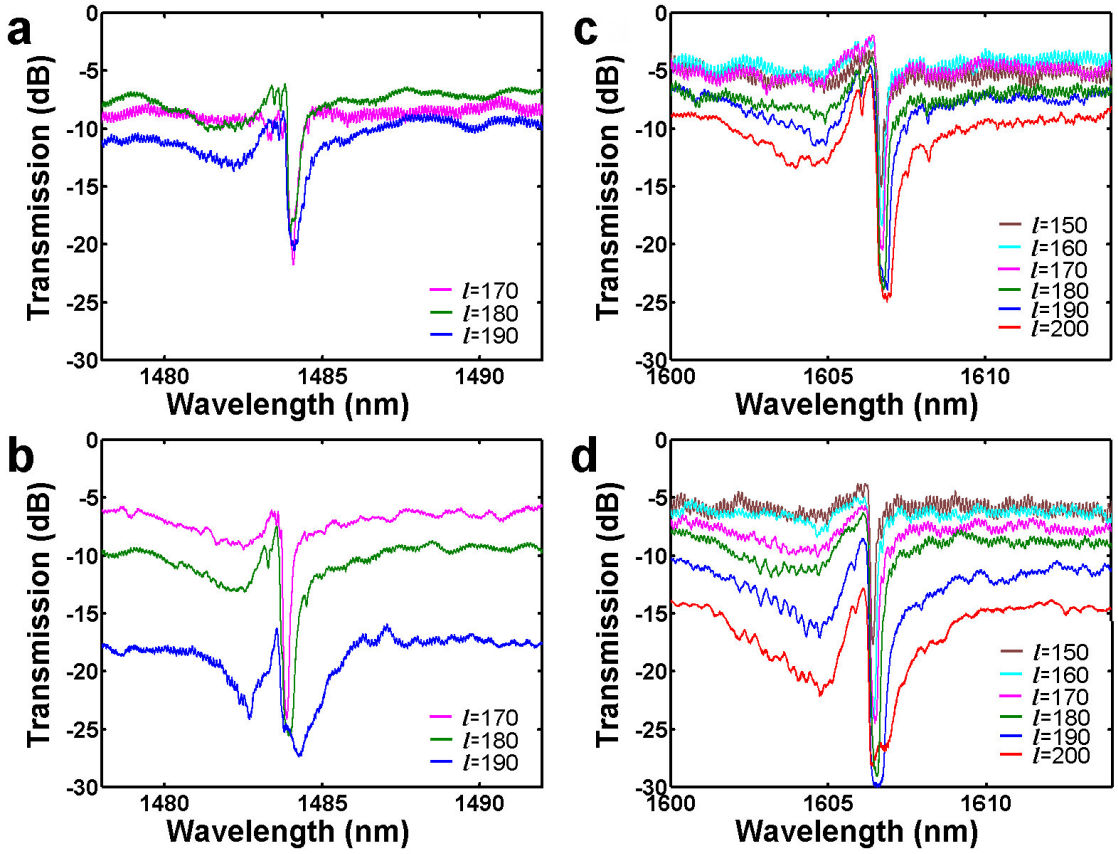

Figure 3. Transmission spectral response of the MM Bragg grating assisted waveguide, like that depicted in Figure 2a, for different length of cut-wires. a) $\Lambda_z = 230$ nm, air overclad. b) $\Lambda_z = 230$ nm, water (n = 1.35) overclad. c) $\Lambda_z = 250$ nm, air overclad. d) $\Lambda_z = 250$ nm, water (n = 1.35) overclad.

3. Coupled-mode-theory phenomenological model

We now present a coarse model of the observed EIT-type behavior based on Coupled-Mode-Theory (CMT). We use two sets of two modes as the basis, each set being naturally bidirectional, thus a 4×4 CMT is used.

The first two modes are classical modes of DFB ridge lasers with a real or complex periodic modulation of the refractive index. The underlying profile is simply pinned by the ridge (relative confinement factor ~10%), and the periodic modulation is felt only close to the ridge-substrate corner regions, due to the periodic gold wires of period Λ. This mechanism is responsible for the classical feedback between the two modes with a propagation constant k.

The other two modes are induced by the MM. They are assumed to essentially behave as guided modes, but their underlying profile corresponds to a field confined beneath the two MM areas of Figure 1. We can consider both sides collectively and restrict ourselves only to modes with an even electric-field profile along x, mainly because those modes with odd transverse profiles do not interact with the even transverse profile of MM z-periodicity (coupling cancellation).[45] The role of the MM transverse resonance is to build-up a frequency-dependent loss. From the studies of model waveguides with the same vertical (y) profile as the one beneath the MM, we have identified that the MM resonance manifests itself on the blue side of the DFB resonance for our range of parameters. Thus we shall parametrize this "MM-guided" mode (MM mode in short) accordingly.

The last key ingredient is the coupling between the two sets of modes. Here, we implement a weakly non-unitary treatment for the cross-terms coupling DFB and MM. The exchange between them is mediated by their tails and by the grating.

The propagation constants k of these four modes in the feedback-free limit enter in the generic phase term $\varphi = k\Delta z[2\pi] = (\omega - \omega_{ref}) n_{eff} c^{-1} \Delta z$. We need only specify the constant $n_{eff} c^{-1} \Delta z$ of each mode corrected by additional factors to normalize the frequency shift $(\omega - \omega_{ref})$ at our choice (here we have set the slope of basic lasers mode at exactly 200=δ/Re(k). Also we define the matrices for a segment length Δz~L/1000 a choice ensuring numerical convenience, unlike the actual period Λ_z ~ L/15000, yet allowing most critical quantities of the CMT to be linearized for analytical exploitation in the future). We denote φ_D the phase of the DFB mode and φ_M the phase of the MM mode.

Before we give more details, we indicate the rest of the procedure. The scattering matrix depicting the energy exchanges of these four modes is analyzed in terms of eigenvalues and eigenmodes onto the small above-mentioned range Δz. The eigenvalue analysis directly gives the modal dispersion $k(\omega)$, real and imaginary. By transformation (basis change) of the desired input onto the eigenmodes, followed by the trivial diagonal propagation of the latter, and the reverse transform, we get the transmission matrix, and thus the transmission/reflection behavior of the system when excited by the sole (experimental) DFB port. We make use of the scattering matrix formalism to avoid the classical numerical overflow of the direct matrix approach, with the direct matrix obtained for an intermediate length L' such as $L' = L/3$, and an application of the appropriate scattering matrix combination rules. The basic scattering matrix S_Δ in the basis {DFB(forward/backward) (MM forward/backward)} reads:

$$S_\Delta = \begin{pmatrix} tC & rC & t_M S & r_M S \\ -rC & tC & -r_M S & t_M S \\ -tS & -rS & t_M C & r_M C \\ rS & -tS & -r_M S & t_M C \end{pmatrix} \begin{pmatrix} e^{i\varphi_D} & 0 & 0 & 0 \\ 0 & e^{i\varphi_D} & 0 & 0 \\ 0 & 0 & e^{i\varphi_M} & 0 \\ 0 & 0 & 0 & e^{i\varphi_M} \end{pmatrix} \begin{matrix} \text{DFB forward}'' \\ \text{DFB backward} \\ \text{MM forward} \\ \text{MM backward} \end{matrix} \quad (1)$$

The 2×2 diagonal blocks of DFB and MM are clearly visible. Here, t and r depict the scattering fate of DFB modes without interaction with MM modes. Similarly, t_M and r_M depict the scattering fate of MM modes without interaction with DFB modes. The crucial DFB-MM coupling is described by C and $S << C$. In a unitary case, we would use $S^2 + C^2 = 1$. However we use a slightly different choice. We parametrize $C = \cos(\theta)$, and $S = (\sin(\theta))^q$ with a power $q = 0.92$ close to unity and $\theta << 1$ a mixing angle for the length Δz. This would amount to asymmetric coupling of DFB and MM in the more classical transmission matrix picture, which could be expected in geometries like ours with coupling coefficient integrals that could differ in an explicit DFB-MM CMT framework.

The transmission coefficients account for the loss processes parametrized by two values $\ell_D << \ell_M << 1$ with simple algebra:

$$t = (1 - \ell_D)\sqrt{1 - r^2}; \quad t_M = (1 - \ell_M)\sqrt{1 - r_M^2} \quad (2)$$

The phases $\varphi_{D,M}$ are built-up from a normalized detuning $\bar{\delta} \propto n_{eff,D,M}(\omega - \omega_{D,M})$ as outlined above, with here ω_D the Bragg DFB frequency through appropriate constants (δ_M, A_M, A). They are algebraically of the form $\varphi_D = \bar{\delta} A + \pi$ and $\varphi_M = (\bar{\delta} - \bar{\delta}_M) A_M + \pi$ with $\bar{\delta}_M$ and A_M / A giving the convenience of expressing the refractive index difference and dispersion difference in normalized units. A set of five values of these parameters is selected by mitigating the desired similarity to the experimental data on the one hand, and a quest for a synthetic

phenomenological rendering, controlled by a single "cursor" much as the wire length l does in the data on the other hand. Henceforth, we do not attempt to connect this parametric level to the exact optogeometric details. [More details are presented in Section. S2 (Supporting Information).]

The first point is to comment the modeled dispersion relations, shown in **Figure 4**. We do this on the most extreme case of water covered MM WG with grating longitudinal period $\Lambda_z = 250$ nm. We add the dispersion of the uncoupled DFB modes (C=1, S=0) as a reference (dark green line).

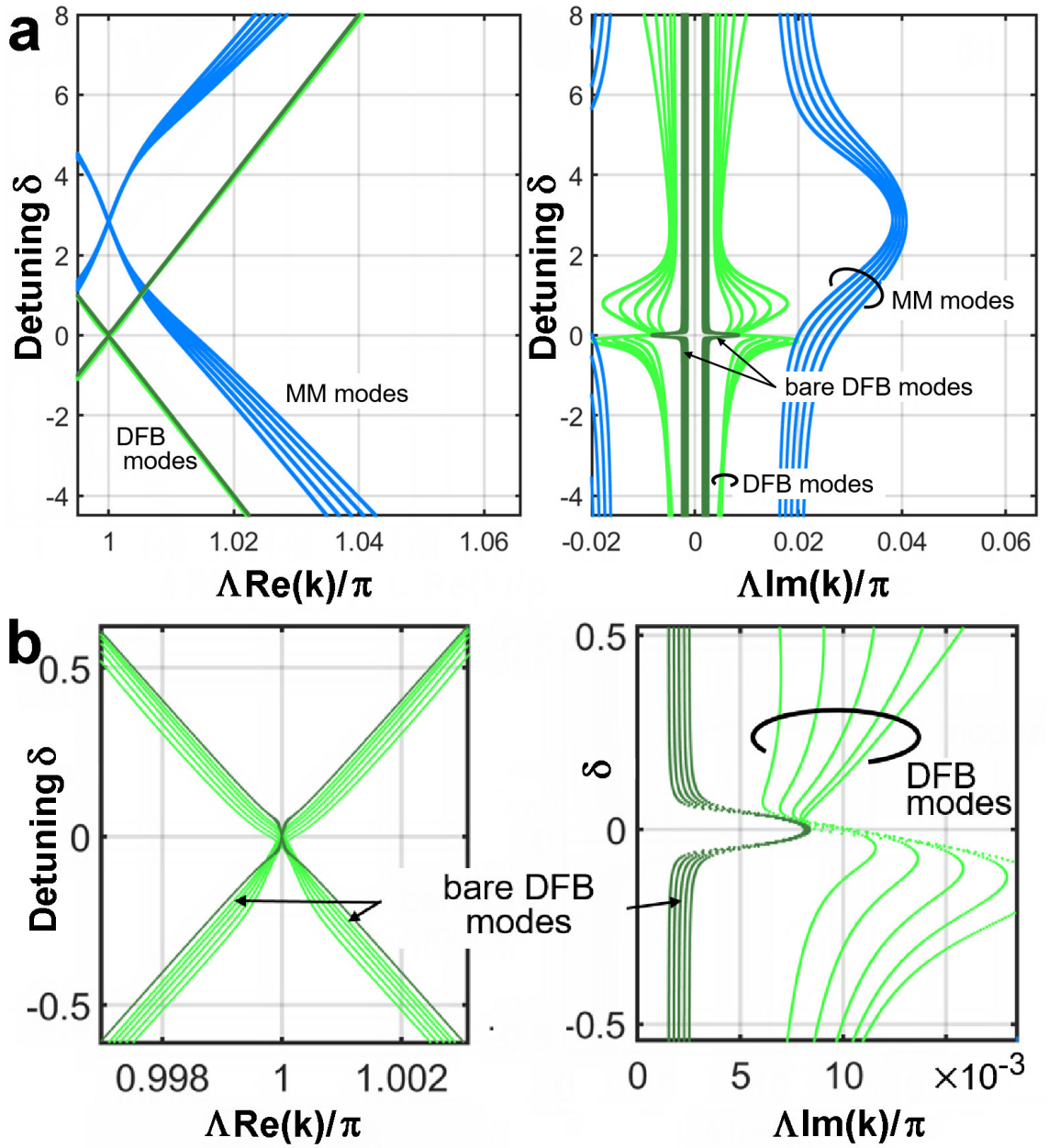

Figure 4. Complex dispersion relations of the four modes under the collective linear variation of a few MMG-related parameters. The arbitrarily normalized detuning δ is here such that a ~2 nm detuning step corresponds to δ = 1. a) Real and imaginary parts of $k(\omega)$. b) Magnified view of complex $k(\omega)$ in the vicinity of EIT region. The DFB mode is shown as a dark green lines/points.

The DFB mode (green curves) is impacted by losses and hybridization to the MM mode. It does not show a proper stop band on the real part $\mathrm{Re}(k)$ at $\Lambda\,\mathrm{Re}(k)=\pi$ (unlike the uncoupled DFB, see Figure 4b), while the structure of $\mathrm{Im}(k)$ for this DFB mode (green curves) readily shows the build-up of the EIT feature. As for the MM mode, it crosses the $\Lambda\,\mathrm{Re}(k)=\pi$ folding axis at $\delta\approx 2.7$, hence ~7 to 9 nm away from the DFB, at almost constant frequency. The MM losses feature first a background losses $\Lambda\,\mathrm{Im}(k)\sim 0.02$ (associated to a $\sim 100\Lambda$ decay length), and also a bump on $\Lambda\,\mathrm{Im}(k)$ that represents their feedback-induced attenuation, which accounts for a similar amount to the losses (since the bump height also verifies $\Lambda\,\mathrm{Im}(k)\sim 0.02$). The interplay of both modes is thus clarified. As can be seen on the green curves (DFB mode), the DFB-MM coupling mainly translates, on the $\delta>0$ side, into an attenuation peak that borrows the initial rise of the MM's loss behavior with δ till $\delta\sim 0.7$, but vanishes when the degrading phase-matching condition prevents the coupling ($\delta>1$). Hence, the observed DFB imaginary band structure is not strongly dependent on the exact MM dispersion features beyond the concerned range ($\delta<1$). It suffices that the interplay of coupling and losses are in the proper proportions to trigger the appearance of a strong dip on the $\delta>0$ side of the initial DFB dip, separated by a peak transmission of EIT nature. At this EIT point, the transfer to the MM mode and the back transfer are balanced in such a way as to minimize the loss in the MM, just as in the principle of standard EIT.
We now present the transmission data themselves, in dB, and compare them to experimental data from water-clad case, where the more extreme forms of EIT are observed. We see that the evolution of the EIT peak value, the typical swing of the transmission, and the transmission shapes are reasonably well rendered by our chosen parametric variation (in our phenomenological equivalence).

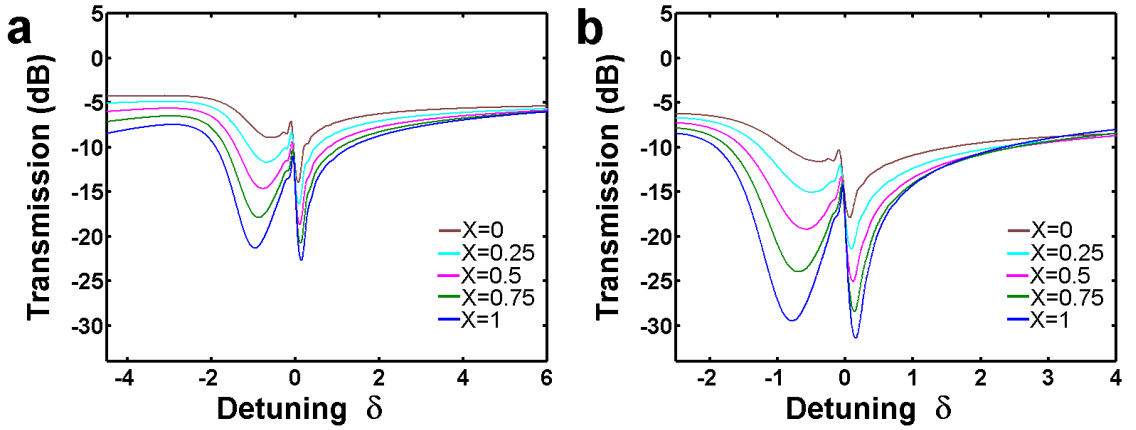

Figure 5. Phenomenological CMT modeling transmission of MM Bragg grating assisted waveguide. The X parameter is a proxy to account for five different lengths of the wires, $l=150$ to $l=190$ nm a) $\Lambda=230$ nm, air overclad. b) $\Lambda=230$ nm, water (n = 1.35) overclad. Note the backward δ axis chosen to correspond to bare wavelength spectra.

In Figure 3b, we only have three experimental curves, while in Figure 3d we have five experimental curves, with a quite reasonable similarity in all respects. For both sets ($\Lambda_z=230$ nm and $\Lambda_z=250$ nm), the EIT peak first slightly diminishes as we go to the more resonant l values, but it eventually tends to resist to further lowering. The last (third) value of l in the $\Lambda_z=230$ nm experiment is probably affected by an issue that we could not identify,

that diminishes its overall transmission and pushes the asymmetry around the EIT to the favor of the $\delta < 0$ (red) side. Within our choice of a gentle parametric behavior in the phenomenological CMT model of **Figure 5a** and 5b, we can only account well for the shape of this peak, but not for the precise shapes of its two side dips.

We feel that experimental data are partly responsible for the remaining discrepancies. Combined with the coupling uncertainties, it is difficult to get more reproducible results, but we believe that the favorable comparison proposed in Figure 5 from our simple phenomenological model does properly make the case for a *bona fide* observation of the EIT phenomenon with a MMG feedback medium. Yet, the model tells us a lot on the physical understanding, especially on Figure 4b. As noted above, the bare MM resonance is far away from the observed dips, we only see the onset of its losses due to the WG/MM coupling. This coupling fades faster than the losses increase as δ increases. Besides Figure 4d makes it obvious that the bare DFB interaction is much enhanced due to the transfer of energy/amplitude to the MM, in a way that is characteristic of the essence of EIT physics. This insight is particularly welcome to orient the future investigations and help modelling and measurement of EIT passive systems of the novel kind presented here to be fully coincident.

4. Demonstration of electrically injected MMG DFB lasers exploiting EIT resonance

As mentioned above, the occurrence of EIT in MMG WG opens perspectives for its application in active type devices such as DFB lasers. The high-contrast narrow transmission band may provide an advantage toward more robust single-frequency operation for DFB lasers. To prove the validity of the present flavor of EIT concept, the same heterostructure that served for the passive MMG WG study was also used for the fabrication of an "EIT laser" with an emission wavelength around 1.24 µm. The essential differences with respect to the passive type MMG WG are: i) an MMG design adapted for operation around 1.24 µm, notably a period $\Lambda_z = 210$ nm; ii) the implementation of a benzocyclobutene (BCB) cladding and a top contact for electrical current injection. Additional details on passive and active MMG devices technological fabrication process are presented in Section S3 (Supporting Information). As for passive MMG WGs, no grating-assisted WGs and only metal Bragg-assisted WGs were also included in the mask layout of active MMG devices.

The emission spectra for a MMG laser with longitudinal period $\Lambda_z = 210$ nm and cut-wire length $l = 160$ nm, $w = 120$ nm, $h = 50$ nm at different injection currents are shown in **Figure 6a**. They display a clearly visible EIT feature, especially when the injection current is below the threshold, which is around I_{th} =21 mA. The laser emission line grows exactly at the sub-threshold local emission maximum, emerging within a few nm wide dip attributed to the MMG. The laser emission is single frequency with a side mode suppression ratio (SMSR) greater than 50 dB up to the largest current ($I \sim 3I_{th}$). Note that outside the EIT region, the width of what appears on the bottom of various graphs as blue curves of irregular thickness are actually the envelopes of amplified spontaneous emission (ASE) that are not resolved at this low magnification. As expected, the ASE amplitude increases with injection current. It can also be observed that in agreement with previous results observed for passive structures, the ASE inside the EIT region remains depressed, especially at the bottom of the dip. The suppression of the ASE in the vicinity of the laser emission wavelength is due to the resonance absorption of the MMG outside the maximum spectral region of the EIT. It provides thus more robust single-frequency laser emission and it is expected to result in reduced ASE noise contribution.

To further consolidate these assertions, the above results are compared with those of a metallic Bragg grating DFB laser from the same cleaved bar of 1.68 mm length. The emission spectra at different injection currents are shown in Figure 6b. As can be seen, soon after the threshold, a second laser line emerges, and is fully developed at an injection current of around

33 mA (fifth spectrum from the left). At variance with the MMG laser the ASE is now maximal in the near vicinity of laser emission lines and its intensity is also considerably higher. Another interesting feature that can be observed in the leftmost spectrum at I = 11.4 mA < I_{th} is that the emission spectrum of metal grating DFB laser shows a tiny ~3 dB dip around 1239 nm. This corresponds to increased absorption of the metallic Bragg grating. The further increase in gain at I > I_{th} leads to laser emission emerging at this very wavelength. This result is entirely consistent with the basic theory of this type of DFB lasers. It highlights the fundamental difference compared to the behavior of the MMG laser whereby the emergence of laser emission occurs at the maximum of the EIT. Additional results illustrating the onset of lasing and the ASE behavior of these lasers are presented in Section S1 (Supporting Information).

To further assess the performances of MMG lasers in terms of emission power and tolerance to parasitic optical feedback, we considered a more conventional DFB laser heterostructure, like that used for the demonstration of the Parity-Time symmetric DFB laser emitting toward 1.55 µm wavelength (in this range, our optical feedback assessment tools are more mastered).[46] It consists of a 2-quantum well (QW) active layer embedded in an InGaAsP separate confinement heterostructure (SCH), grown by Gas Source Molecular Beam Epitaxy (GSMBE). The design of its MMG was also adapted for the operation at this wavelength.

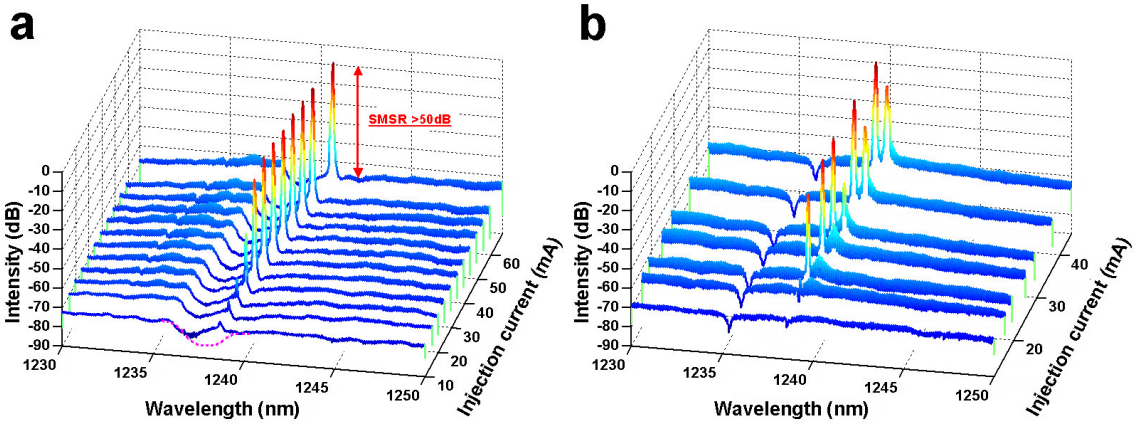

Figure 6. Emission spectra of 1.68 mm long laser waveguide structures. a) MMG laser (injection currents: I = 10, 15.3, 19.6, 24.5, 29.4, 34.3, 39.2, 44.1, 49, 53.9, 58.8, 68.6 mA). b) Metallic Bragg grating DFB laser (injection currents: I = 11.4, 16.1, 19.1, 24.8, 28.9, 36.8, 45 mA).

The emission spectra for different injection currents up to 200 mA for two devices from the same cleaved bar, a MMG and a metal Bragg grating DFB lasers, are shown respectively in the **Figure 7a** and 7b. Both thus feature 1.36-mm-long cavities, and they are soldered on a copper heat sink. As can be seen, both lasers exhibit excellent single frequency emission with SMSR > 50 dB. However, the light-current diagram in Figure 7c shows that the optical power emitted by the MMG laser (23 mW at 200 mA) is significantly higher than that of the DFB metal grating (13 mW at 200m A). The threshold current of the MMG laser is also lower, 18.2 mA compared to 24.2 mA for its metal grating counterpart. Further increase of emitted power could be achieved by considering top-down laser soldering, enhancing thermal dissipation.

As a crucial test towards real-world applications, the resistance of MMG laser to external optical feedback was investigated under the same protocol as conventional metallic grating DFB lasers. The measured parameter is the so-called optical return loss (ORL), the smallest optical return loss that impairs the laser coherence. It manifests as the spectral broadening of the laser emission line, the so-called laser coherence collapse. Relatively high tolerance to

optical feedback is usually achieved by the use of an active medium which ensures high differential gain and low linewidth enhancement factors.[47 and references therein]

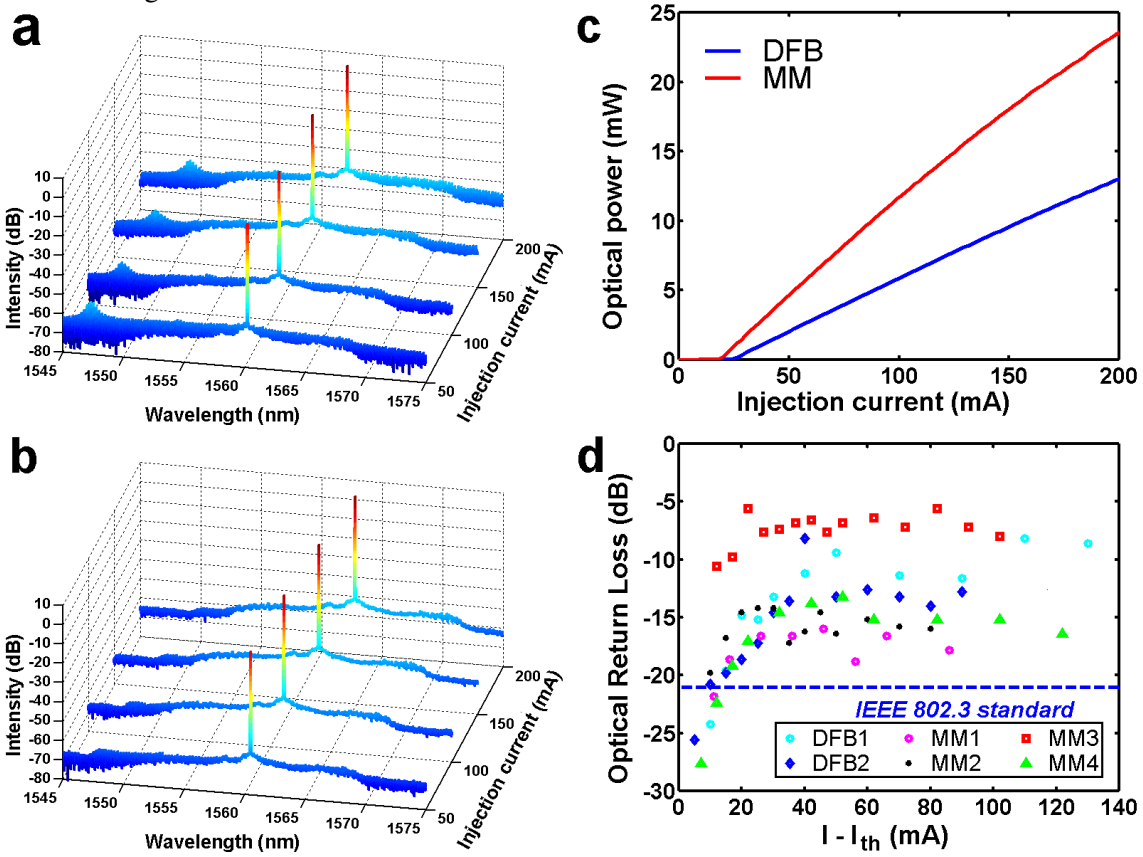

Figure 7. a) Emission spectra of 1.36 mm long MMG laser with grating parameters $\Lambda_z = 242$ nm, $l = 220$ nm, $w = 120$ nm, $h = 50$ nm, (injection currents: I = 50, 100, 150, 200 mA); b) Emission spectra of 1.36 mm long metallic Bragg grating DFB laser with period $\Lambda_z = 242$ nm (injection currents: I = 50, 100, 150, 200 mA); c) Light power characteristic of 1.36 mm long MMG and metallic Bragg grating DFB lasers with period $\Lambda_z = 242$ nm. d) Resistance to external feedback of MMG and metallic Bragg grating DFB lasers, showing the high ORL levels of MMG lasers.

The measurements of ORL performed for MMGs and DFBs are summarized in Figure 7d. Despite a sizable dispersion of the results, all the lasers tested reach high enough ORL levels to comply with the IEEE 802.3 standard without an isolator, which requires ORL above -21 dB. The onset of coherence collapse can reach as much as - 5.6 dB for the most robust MMG laser while the median ORL value for the ensemble is around - 14 dB. The grating parameters of tested lasers and the peak emitted power (P_{max}) are gathered in Table I.

Table 1. Parameters of MMG and metallic grating DFB used in ORL measurements

Laser code	DFB1	DFB2	MM1	MM2	MM3	MM4
Λ_z (nm)	240	240	238	240	240	242
l (nm)	-	-	220	180	210	220
P_{max} (mW)	7.7	13	14.5	18	14	23

The MMG laser linewidth has finally been assessed and compared to that of the DFB-metal grating only ones. A standard self-heterodyning technique has been used for the linewidth measurement of several lasers and comparison was made for lasers of the same cavity length (L=1.36 mm).
The DFB-metal grating device showed a linewidth of about 7 MHz for an output power of 8 mW while that of the MMG device amounted to 3 MHz for the same output power, a state-of-the-art value. The narrower MMG laser linewidth can be attributed to the additional EIT filtering effect since for the rest of parameters the two lasers are identical.

4. Summary and conclusions

In this study we investigated the behavior of active and passive WGs whose frequency selection is assisted by a MMG operated in the NIR domain. We report the observation in passive type WGs of a marked Fano type EIT effect with record high quality factor of resonance: Q ~ 5000 and contrast >20 dB. Unlike any standard metal grating, MMG assisted waveguides simultaneously exhibit both strong grating coupling strength and low-loss properties. Though theoretically predicted,[44] experimental demonstration of this effect does not seem to be hitherto reported.
This concept is further applied to the demonstration of single frequency emitting electrically injected DFB lasers exploiting a resonant enhanced transmission due to the EIT first at $\lambda \sim 1.24\mu m$, then at $\lambda \sim 1.55\mu m$. It addresses in this way one of the main critical issues of conventional DFB lasers related to their single frequency yield.
The occurrence of EIT in a MMG assisted waveguide brings a lot of advantages that trigger a new paradigm for DFB lasers. We experimentally demonstrate that the onset of laser emission with the increase of injection currents occurs at the peak of EIT, i.e. the maximum in transmission. Other important advantages brought by the MMG DFB laser concept and experimentally demonstrated are: large single-mode yield with SMSR > 50dB, low threshold current < 20 mA, high optical emission power up to 23 mW, tolerance to optical feedback above –21 dB and compliant with the IEEE 802.3 standard without an isolator, enhanced polarization selectivity > 10dB.
The laser performances are at the state-of-the art. The interest of the concept of MMG DFB lasers showcased here is that it is fully compatible with existing industrial technologies and promising for large scale real-life telecom applications. Modifications of various key physical aspects through further tuning of MMG parameters should be further investigated to fruit the full potential of this novel approach. Such highly coherent laser sources are indeed required in diverse applications as coherent communications, sensing, programmable photonic circuits,…

Acknowledgements

This work was partially funded by the Labex NanoSaclay project DISYPTE, CNRS INSIS prematuration project LACOMETA, BpiFrance IPCEI-CIS project METAGRAAL (LS 262296). VB acknowledges financial support from EDOM “Ecole Doctorale” through a PhD grant. Funding by the China Scholarship Council is acknowledged by Y. L (grant number 201906750021).
This work was done within the C2N micro nanotechnologies platforms and partly supported by the RENATECH network and the General Council of Essonne.
N. Dubrovina and Y. Liang contributed equally to this work

References

[1] J. B. Pendry, "Negative Refraction Makes a Perfect Lens," *Phys. Rev. Lett.* **2000**, 85, 3966-3969.

[2] N. Engheta, "Circuits with light at nanoscales: optical nanocircuits inspired by metamaterials," *Science* **2007**, 317, 1698-1702.

[3] N. Yu, P. Genevet, M. A. Kats, F. Aieta, J. P. Tetienne, , F. Capasso, Z. Gaburro, "Light propagation with phase discontinuities: generalized laws of reflection and refraction," *Science* **2011**, 334, 333-337.

[4] X. Ni, N. K. Emani, A. V. Kildishev, A. Boltasseva, V. M. Shalaev, "Broadband light bending with plasmonic nanoantennas," *Science* **2012**, 335, 427.

[5] F. Aieta, P. Genevet, M. A. Kats, N. Yu, R. Blanchard, Z. Gaburro, F. Capasso, "Aberration-free ultrathin flat lenses and axicons at telecom wavelengths based on plasmonic métasurfaces," *Nano Lett.* **2012**, 12, 4932-4936.

[6] N. Zheludev, Y. Kivshar, "From metamaterials to metadevices," *Nat. Mater.* **2012**, 11, 917–924.

[7] O. Hess, O., J. B. Pendry, S. Maier, R. F. Oulton, J. M. Hamm and K. L. Tsakmakidis, "Active nanoplasmonic metamaterials," *Nat. Mater.* **2012** 11, 573–584.

[8] L. L. Huang, X. Chen, H. Mühlenbernd, H. Zhang, S. Chen, B. Bai, Q. Tan, G. Jin, K.-W. Cheah, C.-W. Qiu, J. Li, T. Zentgraf, S. Zhang, "Three-dimensional optical holography using a plasmonic metasurface," *Nat. Commun.* **2013**, 4, 2808.

[9] X. Ni, A. V. Kildishev, V. M. Shalaev, "Metasurface holograms for visible light," *Nat. Commun.* **2013**, 4, 2807.

[10] N. Yu, F. Capasso, "Flat optics with designer metasurfaces," *Nat. Mater.* **2014**, 13, 139-150.

[11] G. Zheng, H. Mühlenbernd, M. Kenney, G. Li, T. Zentgraf, S. Zhang, "Metasurface holograms reaching 80% efficiency.," *Nat. Nanotechnol.* **2015**, 10, 308-312.

[12] A. F. Koenderink, A. Alù, A. Polman, "Nanophotonics: Shrinking light-based technology," *Science* **2015**, 348, 516-521.

[13] F. B. Arango, A. Kwadrin, A. F. Koenderink, "Plasmonic antennas hybridized with dielectric waveguides," *ACS Nano* **2012**, 6, 10156-10167.

[14] I. Staude, M. Decker, M. J. Ventura, C. Jagadish, D. N. Neshev, M. Gu, and Y. S. Kivshar, "Hybrid High-Resolution Three-Dimensional Nanofabrication for Metamaterials and Nanoplasmonics," *Advanced Materials* **2013**, 25(9), 1260-1264.

[15] M. Chamanzar, Z. Xia, S. Yegnanarayanan, A. Adibi, "Hybrid integrated plasmonic-photonic waveguides for on-chip localized surface plasmon resonance (LSPR) sensing and spectroscopy," *Opt. Express* **2013**, 21, 32086-32098.

[16] S. R. K. Rodriguez, Y. T. Chen, T. P. Steinbusch, M. A. Verschuuren, A. F. Koenderink, J. Gómez Rivas, "Light-Emitting Waveguide-Plasmon Polaritons," *Phys. Rev. B* **2014**, 90, 235406.

[17] A. H. Schokker, A. F. Koenderink, "Lasing at the band edges of plasmonic lattices," *Phys. Rev. B* **2014**, 90, 155452 .

[18] R. Guo, M. Decker, F. Setzpfandt, I. Staude, D. N. Neshev, Y. S. Kivshar, "Plasmonic Fano nanoantennas for on-chip separation of wavelength-encoded optical signals," *Nano Lett.* **2015**, 15, 3324-3328.

[19] R. Bruck, O. L. Muskens, "Plasmonic nanoantennas as integrated coherent perfect absorbers on SOI waveguides for modulators and all-optical switches," *Opt. Express* **2013**, 21, 27652-27671.

[20] Y. Fan, X. Le Roux, A. Korovin, A. Lupu, and A. de Lustrac, "Integrated 2D-graded index plasmonic lens on a silicon waveguide for operation in the near infrared domain," ACS Nano **2017**, 11(5), 4599-4605.

[21] Y. Meng, Y. Chen, L. Lu, Y. Ding, A. Cusano, J. A. Fan, Q. Hu, K. Wang, Z. Xie, Z. Liu, Y. Yang, Q. Liu, M. Gong, Q. Xiao, S. Sun, M. Zhang, X. Yuan and X. Ni, "Optical meta-waveguides for integrated photonics and beyond," *Light: Science & Applications* **2021**, 10(1), 235.

[22] M. Fleischhauer, A. Imamoglu, and J. P. Marangos, "Electromagnetically induced transparency: Optics in coherent media," *Rev. Mod. Phys.* **2005**, 77(2), 633-673.

[23] A. E. Miroshnichenko, S. Flach, and Y. S. Kivshar, "Fano resonances in nanoscale structures," *Rev. Mod. Phys.* **2010**, 82 (3), 2257-2298.

[24] H. Lu, X. Liu, and D. Mao, "Plasmonic analog of electromagnetically induced transparency in multi-nanoresonator-coupled waveguide systems," *Phys. Rev. A* **2012**, 85(5), 053803.

[25] A. B. Khanikaev, C. Wu, and G. Shvets, "Fano-resonant metamaterials and their applications," *Nanophotonics* **2013**, 2(4), 247-264.

[26] M. Rahmani, B. Luk'yanchuk, and M. Hong, "Fano resonance in novel plasmonic nanostructures," *Laser Photonics Rev.* **2013**, 7: 329-3490.

[27] M. F. Limonov, M. V. Rybin, A. N. Poddubny, and Y. S. Kivshar, "Fano resonances in photonics," *Nat. Photonics* **2017**, 11(9), 543-554.

[28] Y.-C. Liu, B.-B. Li, and Y.-F. Xiao, "Electromagnetically induced transparency in optical microcavities," *Nanophotonics* **2017**, 6(5), 789-811.

[29] D. Yu, Y. Bekele, K. Yvind, J. Mork, "In-Plane Photonic Crystal Devices using Fano Resonances," *Laser Photonics Rev.* **2019**, 13, 1900054.

[30] G. Cao, S. Dong, L.-M. Zhou, Q. Zhang, Y. Deng, C. Wang, H. Zhang, Y. Chen, C.-W. Qiu, X. K. Liu, "Fano Resonance in Artificial Photonic Molecules," *Adv. Optical Mater.* **2020**, 8, 1902153.

[31] M. F. Limonov, "Fano resonance for applications," *Adv. Opt. Photon.* **2021**, 13, 703-771.

[32] Y. Yang, I. I. Kravchenko, D. P. Briggs, and J. Valentine, "All-dielectric metasurface analogue of electromagnetically induced transparency," Nat. Commun. 2014, 5, 5753.

[33] F. Zhang, C. Li, Y. Fan, R. Yang, N. H. Shen, Q. Fu, W. Zhang, Q. Zhao, J. Zhou, T. Koschny, and C. M. Soukoulis, "Phase-Modulated Scattering Manipulation for Exterior Cloaking in Metal–Dielectric Hybrid Metamaterials," Adv. Mater. 2019, 31, 1903206.

[34] C. Li, R. Yang, X. Huang, Q. Fu, Y.Fan, and F. Zhang, "Experimental Demonstration of Controllable PT and anti-PT Coupling in a non-Hermitian Metamaterial," Phys. Rev. Lett. 2024, 132, 156601.

[35] H. Soda, Y. Kotaki, H. Sudo, S. Ishikawa, H.and Yamakoshi, and H. Imai, "Stability in single longitudinal mode operation in GaInAsP/InP phase-adjusted DFB lasers," *IEEE J. Quantum Electron.* **1987**, 23(6), 804–814.

[36] M. Usami, S. Akiba, and K. Utaka, "Asymmetric λ/4-shifted InGaAsP/InP DFB lasers," *IEEE J. Quantum Electron.* **1987**, 23(6), 815–821.

[37] G. P. Agrawal and N. K. Dutta, *Semiconductor lasers,* Springer, Science & Business Media, **2013**.

[38] S. Donati and R.-H. Horng, "The Diagram of Feedback Regimes Revisited," *IEEE J. Sel. Top. Quantum Electron.* **2013**, 19, 1500309.

[39] M. Aliannezhadi, F. Shahshahani, and V. Ahmadi, "Improved performance of complex gain-coupled DFB laser by using tapered grating structure," *Opt. Quantum Electron.* **2011**, 44, 1-16.

[40] M. Kamp, J. Hofmann, F. Schafer, M. Reinhard, M. Fischer, T. Bleuel, J. P. Reithmaier and A. Forchel, "Lateral coupling – a material independent way to complex coupled DFB lasers," *Opt. Mater.* **2001**, 17, 19-25.

[41] Y. Nakano, Y. Deguchi, K. Ikeda, Y. Luo, K. Tada, "Reduction of excess intensity noise induced by external reflection in a gain-coupled distributed feedback semiconductor laser," *IEEE J. Quantum Electron.* **1991**, 27, 1732–1735.

[42] K. David, J. Buus, G. Morthier and R. G. Baets, "Coupling coefficients in gain-coupled DFB lasers: inherent compromise between coupling strength and loss," *J. Lightwave Technol.* **1991**, 23, 439-441.

[43] Y. Liang, E. Bochkova, S. Burokur, A. de Lustrac, H. Benisty, A. Lupu, "Engineering of the Fano resonance spectral response with non-Hermitian metasurfaces by navigating between exceptional point and bound states in the continuum conditions," *Opt. Express* **2024**, 32, 7158-7170.

[44] A. Ishikawa, R.F. Oulton, T. Zentgraf, and X. Zhang, "Slow-light dispersion by transparent waveguide plasmon polaritons," *Phys. Rev. B* **2012**, 85, 155108.

[45] S. Olivier, H. Benisty, C. J. M. Smith, M. Rattier, C. Weisbuch, and T. F. Krauss, "Transmission properties of two-dimensional photonic crystal channel waveguides," *Opt. Quantum Electron.* **2002**, 34, 171-181.

[46] V. Brac de la Perrière, Q. Gaimard, H. Benisty, A. Ramdane, and A. Lupu, "Electrically injected parity-time symmetric DFB lasers for telecom applications," *Nanophotonics* **2021**, 10, 1309-1317.

[47] S. Azouigui, B. Dagens, F. Lelarge, J.-G. Provost, D. Make, O. Le Gouezigou, A. Accard, A. Martinez, K. Merghem, F. Grillot, O. Dehaese, R. Piron, S. Loualiche, Q. Zou and A. Ramdane, "Optical feedback tolerance of quantum dot and quantum dash based semiconductor lasers operating at 1.55 µm, " *IEEE J. Sel. Top. Quantum Electron.* **2009**, 15(3), 764-773.

Supporting Information

Electrically injected metamaterial grating DFB laser exploiting an ultra-high Q Electromagnetic Induced Transparency resonance for spectral selection

*Natalia Dubrovina, Yaoyao Liang, Quentin Gaimard, Vincent Brac de la Perrière, Kamel Merghem, Henri Benisty, André De Lustrac, Abderrahim Ramdane, Anatole Lupu**

S1. Experimental characterization methods

S1.1. Electro-optical measurements techniques

To get a full scope of the performances and characteristics of the metamaterial grating (MMG) and metallic Bragg gratings, the WG structures and lasers of all kinds were probed in passive and active configurations, respectively. Measuring the transmitted intensity on passive waveguide (WG) structures assisted by MMG provides the spectral response of the Fano-type EIT resonance, an indication of the coupling strength between the grating and the modes propagating inside the WGs as well as the losses induced by the different types of gratings. The schematic of the optical bench used for transmission measurements on passive WG structures is shown in **Figure S1**.

Three tunable diode lasers from Yenista Optics T100S series with fibered output cover the entire spectral range between 1250 and 1640 nm without interruptions or mode hopping. The light polarization state is controlled by using a pigtailed General Photonics PolaRITE polarization controller and an OZ optics fiber polarization rotator connected with the same supplier's "panda type" polarization maintaining lensed fiber with 2 µm focusing waist. The Elliot Martock optical coupling bench is used to inject light from the lens fiber into the optical waveguide. A Mitutoyo FS70 optical microscope with long focal distance objectives is used to facilitate fiber alignment and select the WG structure to measure. The light transmitted to the WG output end is collected by a 32x long focal distance microscope objective with NA = 0.6. The collimated light is divided by a cube beam splitter toward Hamamatsu IR camera to visualize the WG mode and also transmitted to an optical component tester used here as a generic name for different types of optical power-meters or spectral response characterization devices employed in our study. For passive type measurements, we used a CT400 broadband optical component tester from Yenista Optics which allows rapid and precise acquisition of transmission spectra with a resolution of down to 1 pm.

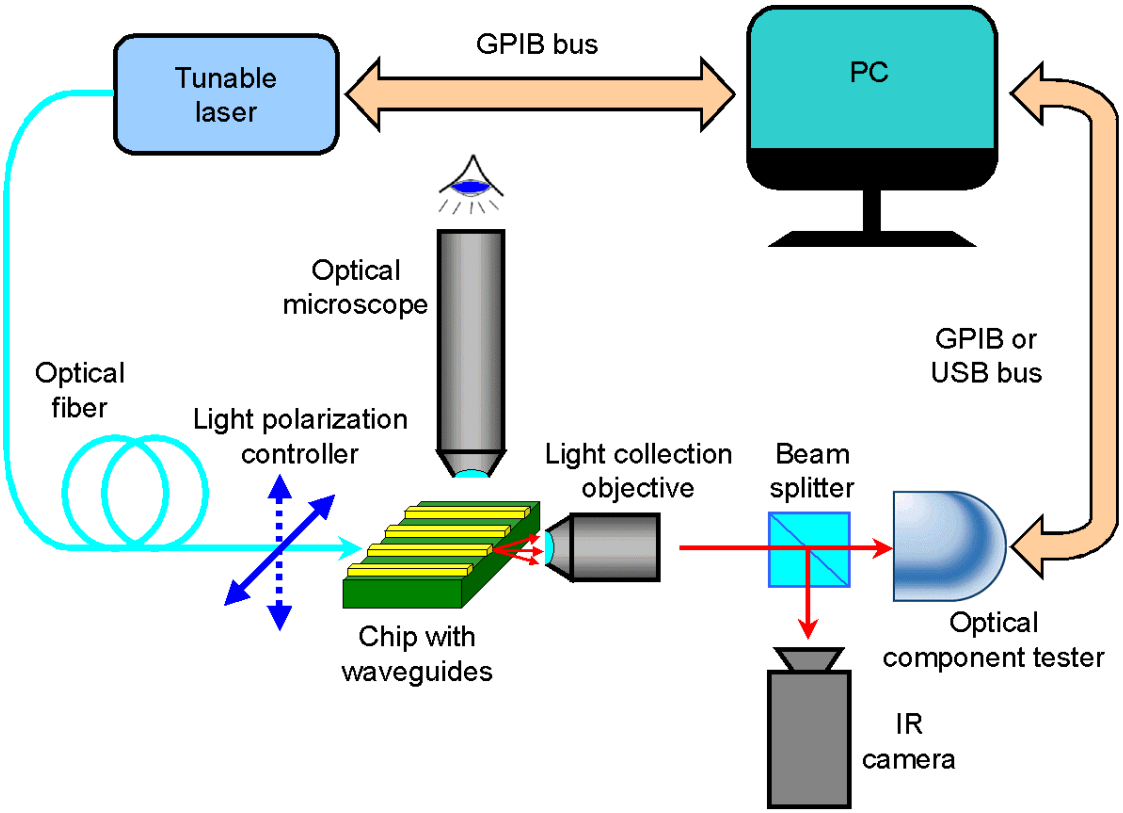

Figure S1. Schematic of the optical bench setup used for transmission spectra characterization.

The same optical bench, but without injection from an external light source, is also used for the electro-optical characterizations of the lasers investigated in our study. To this end, a Karl Suss micropositioner probe head was used to provide injection current by establishing a connection with the laser electrode, with the bottom contact provided by a laser sample holder electrically isolated from the ground. The electric scheme of the setup, used also for light-power characterizations is shown in **Figure S2**.

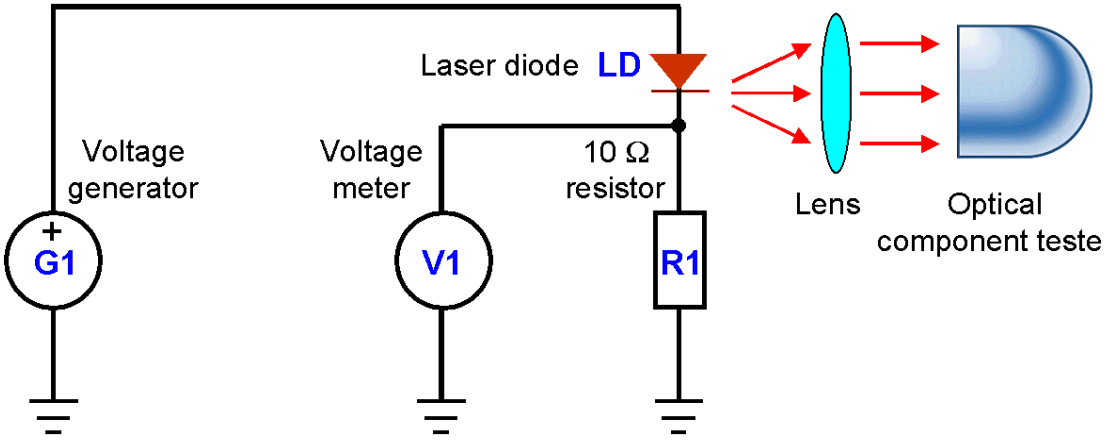

Figure S2. Schematic of the setup used for lasers opto-electronic characterizations.

As an electrical source for voltage supply we used either a TGA1230 waveform generator allowing pulsed operation at a variety of duty cycles or a Yokogawa 7651 DC source. The electrical current in the circuit was determined through the measurement of voltage drop across a 10 Ω resistor R1 (see Figure S2) by means of a Tektronix TDS 360 oscilloscope. The

emitted optical power was measured by means of either a Melles Griot 13PDC001 optical power-meter equipped with an integrating sphere detector or an Agilent 8163A power-meter having a fibered input. The laser emission spectra were characterized by using an ANDO AQ6317B optical analyzer with wavelength resolution down to 10 pm.

S1.2. Polarization selectivity properties of MMG

To highlight the polarization selectivity properties related to the resonant excitation of localized surface plasmons (LSP), we performed transmission measurements of MMG WGs in TM polarization, i.e. when the polarization component of the electric field is along the *y* axis. As can be seen in **Figure S3**, for the same structures as in **Figure 3a** of main text, the transmission spectra do not display any electromagnetically induced transparency (EIT) feature signature. Additionally, the Bragg wavelength drop in transmission is rather low, barely reaching 5 dB, in contrast to up to 20 dB in TE polarization. The distributed feedback (DFB) type metallic Bragg grating assisted WGs show much more pronounced dip in transmission at λ_{Br}, reaching up to 10 dB. This value is similar to that observed in TE polarization.

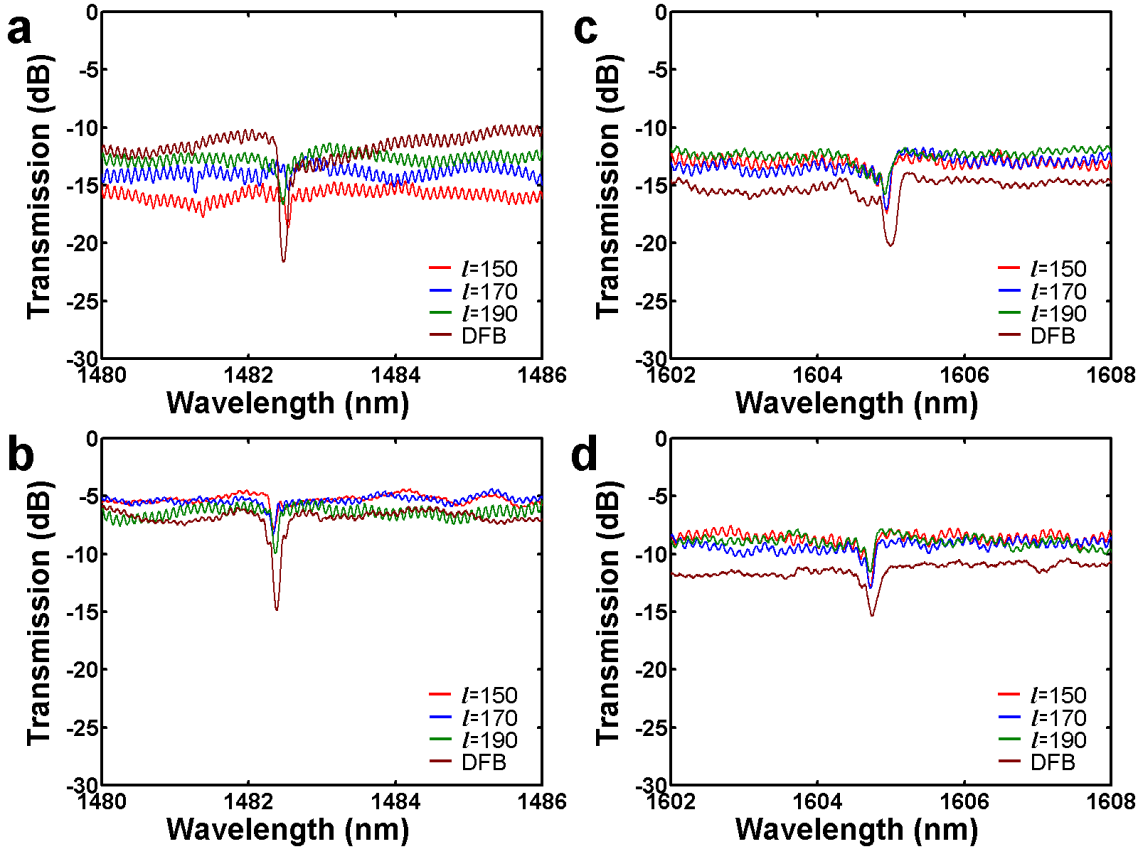

Figure S3. Transmission spectral response of the MMG assisted waveguide in TM polarization for different lengths of cut-wires 150, 170 and 190 nm. The broader DFB type, metallic-Bragg-grating-assisted, WG spectral response is also represented in brown color for the sake of comparison. a) $\Lambda_z = 230$ nm, air overclad. b) $\Lambda_z = 230$ nm, water (n = 1.33) overclad. c) $\Lambda_z = 250$ nm, air overclad. d) $\Lambda_z = 250$ nm, water (n = 1.33) overclad.

S1.3. Comparative study of amplified spontaneous emission behavior

To illustrate the differences in amplified spontaneous emission (ASE) between three different types of lasers investigated in our study, we show in Figure S4 the evolution of their emission

spectrum with an injection current from sub-threshold to above-lasing-threshold regime. As can be observed by inspecting Figure S4a, at an injection current I = 12.3 mA for the MMG laser, there is a visible EIT peak in the emission spectrum. At the same time, for a current value close to I = 11.4 mA, in the spectra of the metal grating DFB laser ("DFB laser" in short), a very narrow drop of approximately 5 dB is observed at $\lambda_{Br} = 1238.5$ nm. The ASE level for the MMG laser is significantly lower than that of the DFB or Fabry-Perot (FP) lasers. With the further increase of the injection current up to I = 16.1 mA, but still below the threshold, an onset of lasing can be observed in Figure S4b for the DFB laser. The EIT peak of the MMG laser also becomes more pronounced. The ASE level whose strength correlates with the amplitude of the FP oscillations is clearly increased for the DFB and FP lasers, but barely so for the MMG laser. A similar situation occurs when the injection current is stronger, around 20 mA. This situation is illustrated in Figure S4c. The DFB laser is already above threshold and shows a single frequency emission line with a side mode suppression ratio (SMSR) > 30 dB. The ASE level is further increased and reaches up to 10 dB for the DFB and FP lasers, but only about 1.5 dB for the MMG one.

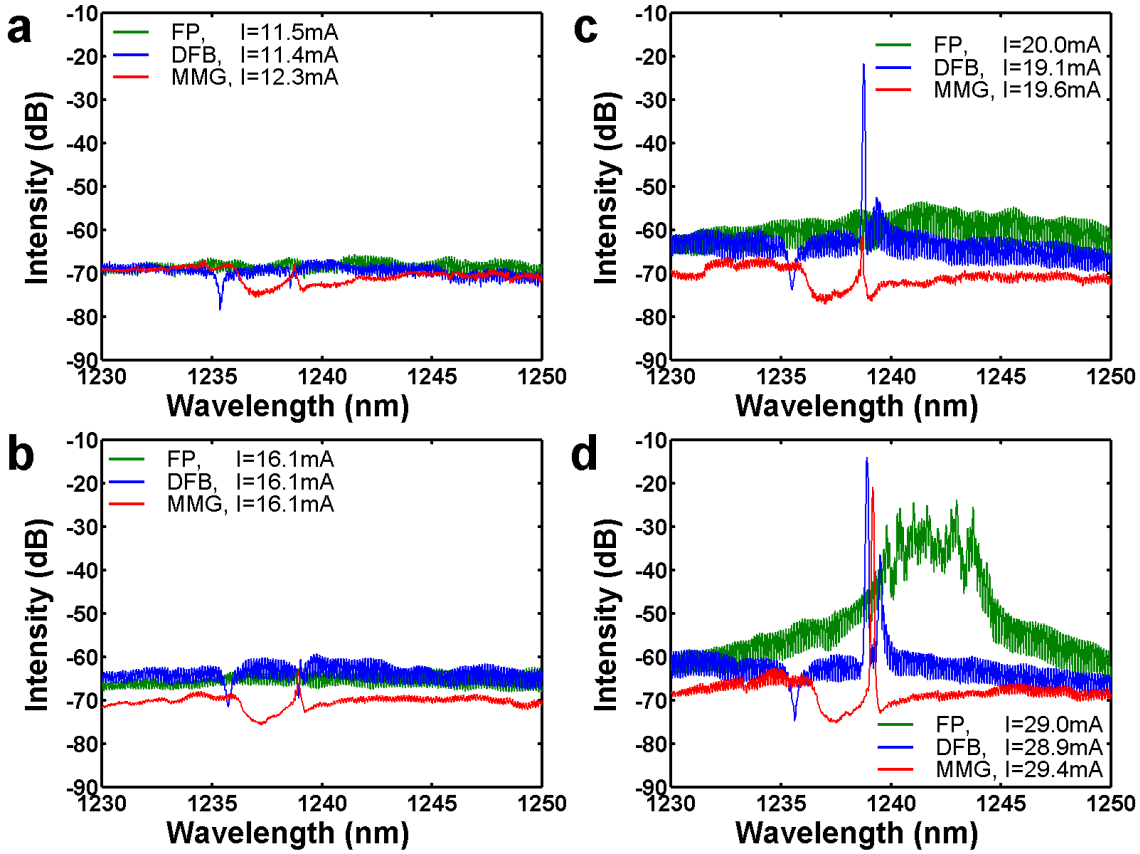

Figure S4. Emission spectra of 1.68-mm-long MMG, metallic-grating-DFB and FP lasers. a) Operation at sub-threshold injection current. b) Operation at near-threshold injection current. c) Operation at near- or just above-threshold injection current. d) Operation well above threshold injection current.

The situation for operation above the threshold when injection current is about 29 mA is represented in Figure S4d. The emission spectrum of the DFB laser is no longer single frequency. In contrast, the MMG laser displays at λ_{Br} a single frequency emission line with SMSR > 40dB. The laser emission occurs within a few nm wide reduced transmission level band corresponding to the MMG absorption. The ASE is still much lower than that of DFB

and FP lasers. Thus, the EIT acts as a narrow-band filter suppressing in this spectral region the amplifications of all cavity modes except one. This feature gives rise to the hope that such types of lasers may present increased robustness with respect to parasitic optical return, which constitutes one of the major impairments of DFB lasers in telecommunications applications.
Note also that despite certain common aspects of the present work with those reported since 2017 on a Fano laser produced on a photonic crystal platform by J. Mørk's team,[1-3] the strategies deployed are very different. The main idea exploited in our work is to use the maximum transmission due to the EIT effect associated with a distributed version of the Fano resonance in order to obtain a narrow-band window of light propagation without loss inside a broadband spectral absorption region, favoring thus a more robust single frequency operation of the laser. In contrast, the main underlying physical mechanism operated in the various realisations of the Fano laser on a photonic crystal platform is to produce a Fabry-Perot resonator that is confined near one of its ends by an spatially entirely distinct auxiliary cavity, possibly with gain, but essentially forming a narrow-band frequency mirror with high reflectivity, and whose detailed operation is indeed of Fano type (specifically, this auxiliary cavity is preferentially coupled at one end, but physically lies somehow on the side, as the photonic crystal modes are more prone to explore the 2D space around their main axis).
Besides the differences in the physical mechanism exploited, the two types of lasers are also radically different with respect to their target applications (long-haul telecommunications versus on-chip communications), their design (plasmonic nanoresonator array versus photonic crystal platforms), their power supply (electric current injection versus optical pumping) and the level of optical power emitted (a few tens of milliwatts versus a few microwatts).

S2. CMT simulation details

We first recall the form of the basic scattering matrix of a short length Δz. In principle, this period could be taken to be the actual period Λ_z. But since $\Lambda_z \sim L/10000$ in typical cases with $L \sim 1.68$ mm the extrapolation becomes numerically more delicate than if we choose, as we do here, to start with the scattering matrix S_Δ for a slightly longer segment $\Delta z \sim L/1500$, still short enough to perform a valid linearization of some basic entries. The matrix S_Δ is given by:

$$S_\Delta = \begin{pmatrix} tC & rC & t_M S & r_M S \\ -rC & tC & -r_M S & t_M S \\ -tS & -rS & t_M C & r_M C \\ rS & -tS & -r_M S & t_M C \end{pmatrix} \begin{pmatrix} e^{i\varphi_D} & 0 & 0 & 0 \\ 0 & e^{i\varphi_D} & 0 & 0 \\ 0 & 0 & e^{i\varphi_M} & 0 \\ 0 & 0 & 0 & e^{i\varphi_M} \end{pmatrix} \begin{matrix} \text{DFB forward} \\ \text{DFB backward} \\ \text{MM forward} \\ \text{MM backward} \end{matrix}$$

where subscript D on the phases are for DFB and M for the MM coupled modes, and r and t (resp. r_M and t_M) are for the transmitted and reflected DFB mode amplitudes of each period (resp. the MM mode amplitudes). The DFB-MM coupling essentially arises from the small S term detailed later.
Both phases can be taken as evolving around the first-order Bragg value π, (i.e. Δz is formally an integer number of period). The frequency-dependence of the phases takes the linear form $\varphi_{D,M} = \mathrm{Re}\left(k_D \Lambda_z\right)\Delta z = \left(\omega - \omega_{ref\,D,M}\right) n_{eff\,D,M} c^{-1} \Delta z$ (we neglect dispersion other than caused by modal interactions). It is also convenient to choose normalized units such that $k_D \Lambda_z$ (the actual phase over one period for the DFB mode) relates to a normalized detuning in the form $\mathrm{Re}\left(k_D \Lambda_z\right) = A\pi\delta$ with a fixed slope $A = 1/200$ (so that $\delta = 100$ corresponds to a "quarter-wave" phase shift) and $\delta_D = 0$ for the DFB Bragg frequency $\omega_{ref\,D}$. The slope of the MM mode is then set by an extra factor close to 1, $A_M = A\left(n_{eff\,M}/n_{eff\,D}\right)$ while its frequency is set by a phenomenological choice of $\delta_M > 0$ (here a few units, see below).

The DFB and MM modes are hybridized by the C, S factors co-directionally only, we neglect DFB/MM contradirectional "cross" feedback. In other words, we assume that the MM role in the feedback is to take some of the DFB mode amplitude in a given direction, to cause contra-directional feedback with the other MM mode, and to couple back to the other DFB mode. We depart from unitarity (i.e. from $S^2 + C^2 = 1$) by a small amount, using $S = (1 - C^2)^{0.46}$. We parametrize C and S by a mixing angle θ. Typically, $C = \cos(\theta)$ and using values of $\theta \in [0.03 \;\; 0.06]$ this raises S from $\sin\theta \in [0.03 \;\; 0.06]$ to $\sin\theta^{0.92} \in [0.048 \;\; 0.090]$. As said in the main text, this could be accounted by asymmetric coupling between the two modes. We did not manage to get a good phenomenological agreement without this transform.

The transmissions in S_Δ are also weak enough to introduce losses in a linearized fashion, $t = (1 - \ell_D)\sqrt{1 - r^2}$; $t_M = (1 - \ell_M)\sqrt{1 - r_M^2}$.

To reproduce five phenomenological curves that reasonably approach the behavior of the three (1484 nm EIT, $\Lambda_z = 230$ nm) or five (1607 nm EIT, $\Lambda_z = 250$ nm) experimental curves, we vary some parameters linearly among five values, in ranges that are close to each other in both 1484 and 1607 nm cases. For this purpose, let us introduce $X \in \left\{0, \frac{1}{4}, \frac{1}{2}, \frac{3}{4}, 1\right\}$

Common to both cases, we have the following variations:

$A_M = (1 + 0.2X)$ (which causes the varying slope of the blue curves in **Figure 4** of main texte);

$\theta = 3 + 3X$.

The variation of A_M is a way to phenomenologically account for a variable degree of coupling domain between the MM and the DFB as a function of the MM wire length parameter, it incurs more room for phase variations and for the attainment of a highly contrasted EIT peak as the dispersions are made to differ in a more pronounced manner (X → 1). The result was more convincing than several other parametric changes attempted.

Going to the specific changes, they are as follows:

for the (1607 nm EIT, $\Lambda_z = 250$ nm) case:

$\delta_M = 3.3$ $\quad \ell_D = (2.5 - X) \times 10^{-4}$ $\quad \ell_M = (20 - 4X) \times 10^{-2}$.

While for the (1484 nm EIT, $\Lambda_z = 230$ nm) case:

$\delta_M = 3.1$ $\quad \ell_D = (2.05 - 0.1X) \times 10^{-4}$ $\quad \ell_M = (18.2 - 0.4X) \times 10^{-2}$.

Finally, the lengths are different so as to adjust phenomenologically to the different values of L/Λ_z, and the different grating confinement factors (essentially defining a "κL product" in classical DFB treatment). We use $L = 1200\Delta z$ for the (1484 nm EIT, $\Lambda_z = 230$ nm) case and $L = 1443\Delta z$ for the (1607 nm EIT, $\Lambda_z = 250$ nm) case.

The rest is standard: we obtain a transmission matrix for a length of typically $400\Delta z$ thanks to the eigenvalues and eigenvectors of the elementary transmission matrix deduced from the scattering matrix S_Δ by usual rules. We then concatenate typically 3 scattering matrices and transmission matrices for the corresponding intermediate lengths to obtain the total scattering matrix. To get the experimental transmission, we simply inject the forward DFB mode by using [1 0 0 0] as the input vector for the four entering waves and get the system transmission as the DFB output port.

S3. Technological fabrication process

The fabrication of the MMG and metallic grating DFB lasers was performed in the clean room of C2N with the expert help of the technical staff. To be in agreement with our wish to apply the EIT-effect-based lasers to practical devices, the processing steps involved in the

fabrication of the MMG lasers were taken as close as possible to the related industry building blocks. The technological fabrication process flow includes several steps of Electron Beam Lithography (EBL), Reactive Ion Etching Capacitively Coupled Plasma (RIE CCP) and Inductively Coupled Plasma (ICP) etching, Physical Vapor Deposition (PVD) for metallic and dielectric deposition processes. The main technological steps are illustrated in **Figure S5**.

Electron beam lithography (EBL) is first used to define alignment marks, the top laser contact, and then the silicon nitride for dry (ICP RIE) etching of the p-cladding layer on the separated confinement heterostructure (SCH). The quality of the etched vertical walls of the WG ridge is shown in **Figure S6a**. Figure S6b illustrates the low roughness of the etched ridge.

After dry etching another EBL step is carried out to perform the insolation of PMMA photoresist for MMG and metallic Bragg grating definition. The precise alignment MMG grating with respect to the ridge WG is obtained using initially defined alignment marks. This EBL represents the most challenging technological step since the definition of precisely and accurate submicron size features on a highly structured surface relief in the near vicinity of the foot of 2 µm height WG ridge "cliff" is not trivial. It required the development of a specific technological process. The precision of the alignments of MMG and metallic Bragg grating with respect to the ridge WG is shown in Figure S6c and 6d, respectively.

The next step is PVD deposition of 50 nm of gold layer followed by a standard lift-off process. The resulting accuracy of thus fabricated metallic Bragg grating and MMG is shown in Figure S6e and 6f, respectively.

The planarization of the WGs is carried out in the next step by spinning and curing the benzocyclobutene (BCB). This is followed by metal electrode deposition on the p side of the sample, thinning and electrode deposition on the n side. All the devices studied are obtained by cleavage of the facets, without specific dielectric coating at this stage.

The technological process for the fabrication of passive WG structures is basically similar but involves less technological steps.

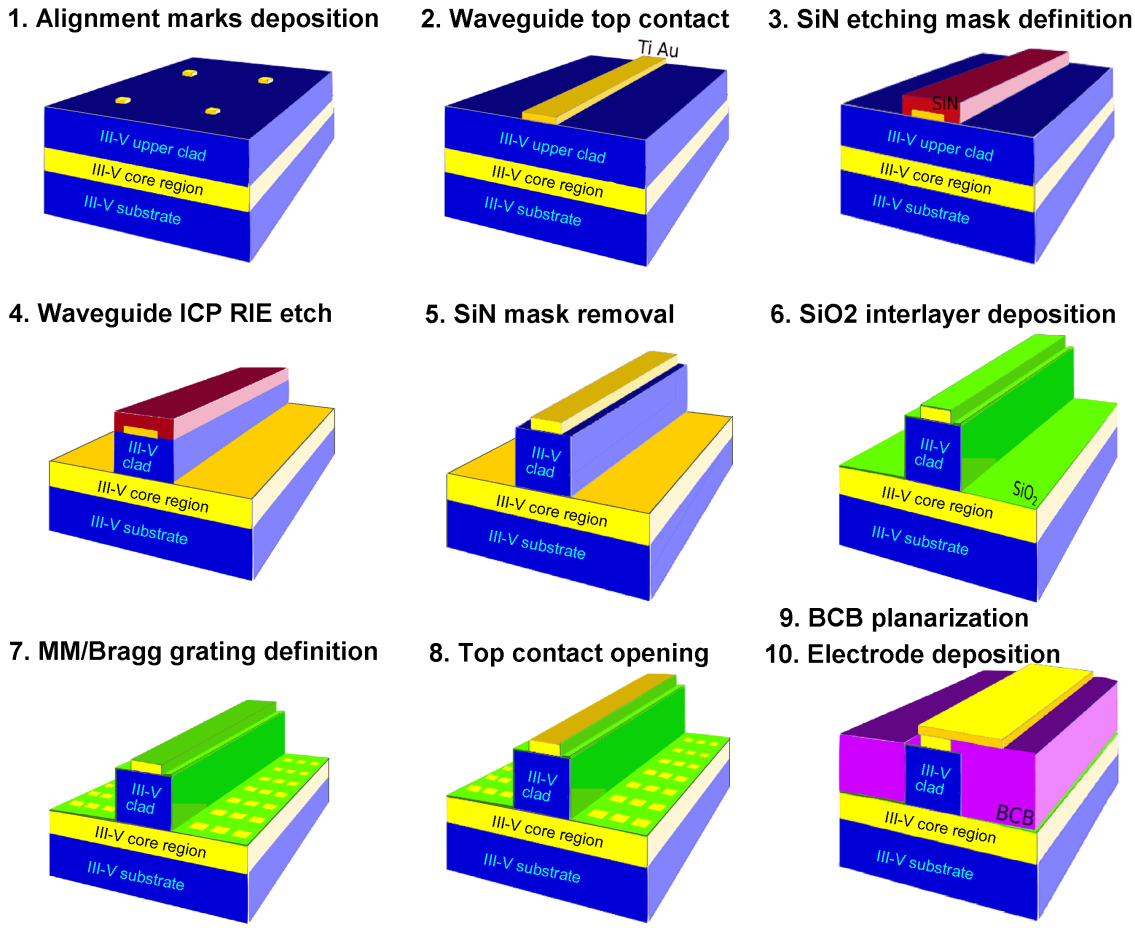

Figure S5. Technological fabrication process flow chart.

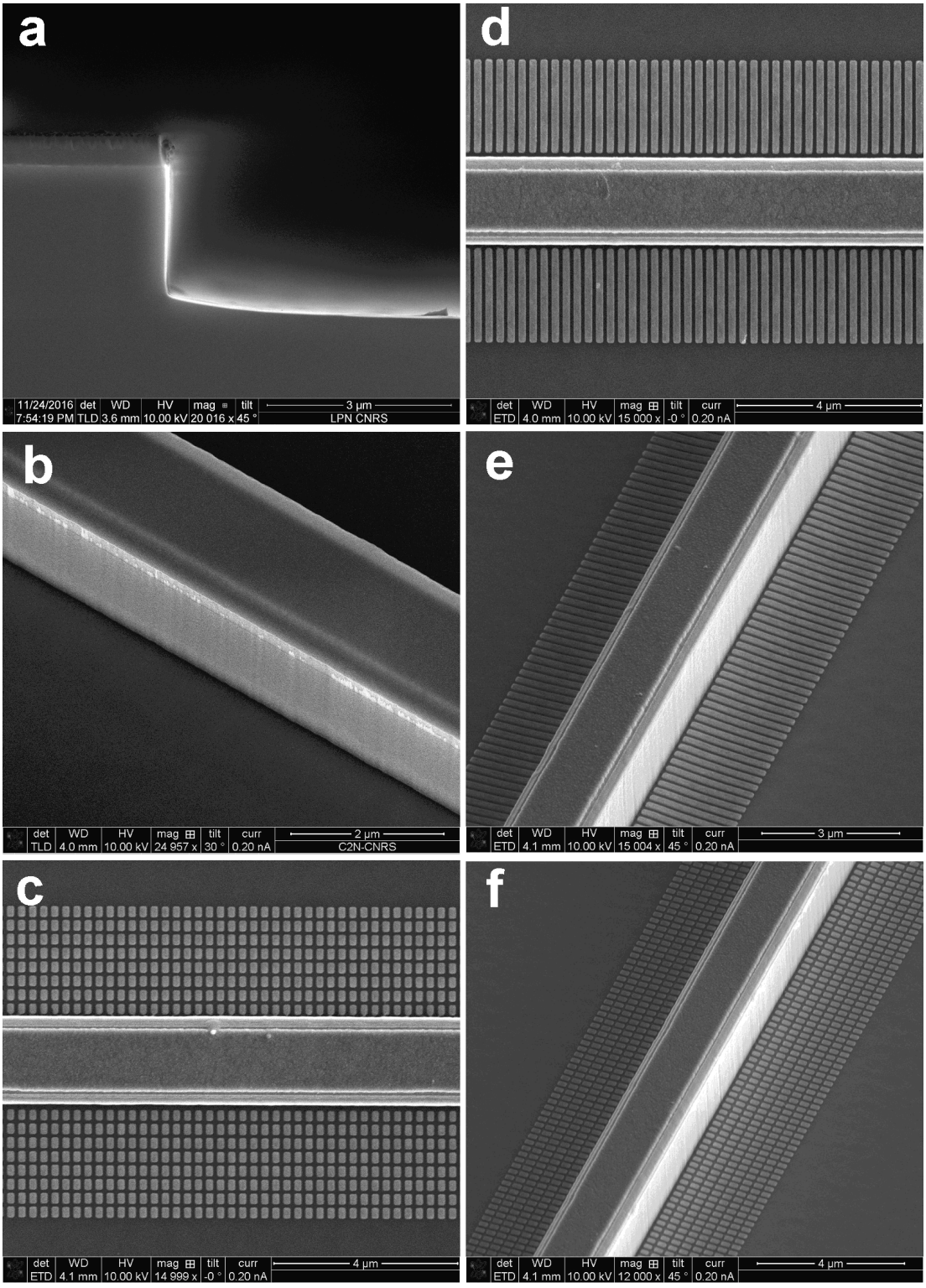

Figure S6. SEM view of devices assessing the quality of technological fabrication process. a) Image of the cleaved facet showing the verticality of etched WG vertical walls. b) Perspective view of WG showing the smoothness of etched ridge vertical walls. c) Top view of etched WG showing the accuracy of alignment of the MMG and top electrical contact. d) Top view of etched WG showing the accuracy of alignment of the of metallic Bragg grating and top electrical contact. e) Perspective view of WG showing the smoothness of etched ridge

vertical walls and the accuracy of fabricated metallic Bragg grating. f) Perspective view of WG showing the smoothness of etched ridge vertical walls and the accuracy of fabricated MMG.

References

[1] Y. Yu, W. Xue, E. Semenova, K. Yvind, and J. Mork "Demonstration of a self-pulsing photonic crystal Fano laser," Nat. Photonics 11(2), 81–84 (2017).

[2] Y. Yu, A. Sakanas, A. R. Zali, E. Semenova, K. Yvind, and J. Mørk, "Ultra-coherent Fano laser based on a bound state in the continuum," Nat. Photonics 15(10), 758–764 (2021).

[3] G. Dong, M. Xiong, E. Dimopoulos, A.Sakanas, E. Semenova, K. Yvind, Y. Yu, and J. Mørk, "Experimental demonstration of a nanobeam Fano laser," Opt. Express 32, 5242-5251 (2024)